SCIENCE CHINA
Life Sciences

•RESEARCH PAPER•

March 2023 Vol.66 No.3: 496–515
https://doi.org/10.1007/s11427-021-2163-1

Deep Sc-RNA sequencing decoding the molecular dynamic architecture of the human retina

Lulin Huang[1,2], Runze Li[1], Lin Ye[1], Shanshan Zhang[1], Huaping Tian[1], Mingyan Du[1], Chao Qu[3], Shujin Li[1], Jie Li[3], Mu Yang[1], Biao Wu[4], Ran Chen[4], Guo Huang[1], Ling Zhong[1], Hongjie Yang[5], Man Yu[3], Yi Shi[1], Changguan Wang[6], Houbin Zhang[1], Wei Chen[4] & Zhenglin Yang[1,2*]

[1]*The Key Laboratory for Human Disease Gene Study of Sichuan Province and the Department of Laboratory Medicine, Sichuan Provincial People's Hospital, University of Electronic Science and Technology of China, Chengdu 610075, China;*
[2]*Research Unit for Blindness Prevention of Chinese Academy of Medical Sciences (2019RU026), Sichuan Academy of Medical Sciences, Chengdu 610075, China;*
[3]*Department of Ophthalmology, Sichuan Provincial People's Hospital, University of Electronic Science and Technology of China, Chengdu 610075, China;*
[4]*School of Ophthalmology and Optometry, Wenzhou Medical College, Wenzhou 325035, China;*
[5]*Department of Organ Transplant Center, Sichuan Provincial People's Hospital, University of Electronic Science and Technology of China, Chengdu 610075, China;*
[6]*Department of Ophthalmology, Peking University Third Hospital, Beijing 100730, China*

Received November 21, 2021; accepted July 13, 2022; published online September 15, 2022

The human retina serves as a light detector and signals transmission tissue. Advanced insights into retinal disease mechanisms and therapeutic strategies require a deep understanding of healthy retina molecular events. Here, we sequenced the mRNA of over 0.6 million single cells from human retinas across six regions at nine different ages. Sixty cell sub-types have been identified from the human mature retinas with unique markers. We revealed regional and age differences of gene expression profiles within the human retina. Cell-cell interaction analysis indicated a rich synaptic connection within the retinal cells. Gene expression regulon analysis revealed the specific expression of transcription factors and their regulated genes in human retina cell types. Some of the gene's expression, such as *DKK3*, are elevated in aged retinas. A further functional investigation suggested that over expression of *DKK3* could impact mitochondrial stability. Overall, decoding the molecular dynamic architecture of the human retina improves our understanding of the vision system.

deep Sc-RNA sequencing, human retina, aging

Citation: Huang, L., Li, R., Ye, L., Zhang, S., Tian, H., Du, M., Qu, C., Li, S., Li, J., Yang, M., et al. (2023). Deep Sc-RNA sequencing decoding the molecular dynamic architecture of the human retina. Sci China Life Sci 66, 496–515. https://doi.org/10.1007/s11427-021-2163-1

INTRODUCTION

Our retina is a marvelous sense organ that allows us to appreciate all the beauty of the world we live in (Kolb et al., 2020). The human retina is a highly specialized photosensitive tissue. It consists of six major neuron cell types: rods and cones (photoreceptors), horizontal cells, bipolar cells, amacrine cells, and retinal ganglion cells (RGCs), each playing a unique role in processing visual signals (Masland, 2012). The human retina also contains three types of glial cells: microglia and two types of macroglia—astrocytes and Müller glia (Reichenbach and Bringmann, 2020). In addition, retinal vascular endothelial cells (VECs) provide blood flow to the retina. The human retina contains a small part

*Corresponding author (email: yangzhenglin@cashq.sc.cn)

called the macular region, where visual resolution is maximized. In addition to the macular area, four quadrants of the retina—nasal, temporal, superior, and inferior—as well as the periphery of the optic cup, form the peripheral retina.

Although the transcriptome of the human retina has been reported using bulk tissue RNA sequencing or single-cell RNA sequencing (scRNA-seq) (Bonnel et al., 2003; Hoshino et al., 2017; Lukowski et al., 2019; Mellough et al., 2019; Wang et al., 2021a), the changes that take place across different regions during aging are poorly understood. Aging has been defined as the progressive accumulation of changes with time that is associated with diseases (Harman, 1981; Huang et al., 2022). Like other tissues, the human retina undergoes aging with reduced functionality (Ungvari et al., 2018). Therefore, age-related loss of retinal function, such as the "mitochondrial theory of aging", is likely to affect retinal physiology (Fletcher, 2010; Wei et al., 2001). Here, we decode the molecular dynamic architecture of the human retina by sequencing over 0.6 million human retinal cells at the single-cell level. This work advances our understanding of the human retina and provides new clues for early intervention in human retinal diseases.

RESULTS

Deconstructing the human retina by scRNA-seq of 0.6 million cells

To generate the transcriptome architecture for human retina tissue at single-cell resolution, retinas from nine unrelated normal eye donors were obtained. All donors were male Han Chinese, aged from 23 weeks of gestation to 81 years old (Figure 1A). For each retina, we dissected it into six sections —nasal, temporal, superior, inferior, macular, and periphery optic cup (Figure 1B). A total of 604,309 qualified cells were obtained for subsequent analyses (Figure 1B). The cell numbers of each of the six regions of the human retina at different ages were presented in Figure 1C and D, respectively. Then, 10 main retinal cell types were identified based on the expression of previously reported markers: rods (*GNAT1*, *NR2E2*), cones (*ARR3*), horizontal cells (*ONECUT2*), bipolar cells (*VSX2*, *VSX1*), amacrine cells (*GAD1*), RGCs (*NEFL*, *NEFM*), microglia (*AIF1*), astrocytes (*GFAP*), Müller cells (*RLBP1*), and VECs (*VWF*) (Figure 1E). The enriched pathways of commonly expressed genes in the 10 human retina cell types were shown in Figure S1A in Supporting Information. These functions are polarly distributed among different regions of the retina (Figure S1B and C in Supporting Information).

Human retina cell subtypes

Phenotypic (and morphalogic) observations have revealed the diversity in human retina neurons (Boycott and Wässle, 1991; Kaneko, 1970). To explore the cell subtypes and their molecular markers in retinal neurons and glia cells (Peng et al., 2019), we performed cell subtype analysis using the scRNA-seq data. Altogether, we distinguished 60 cell subtypes in the human retinas (three cone subtypes, one rod cell type, six horizontal subtypes, 14 bipolar subtypes, 12 amacrine subtypes, 16 RGC subtypes, two astrocyte subtypes, three microglia subtypes, two Müller subtypes, and one VECs) (Figure S2A and B, Table S1 in Supporting Information). Consistent with previous reports (Zhang et al., 2019), three cone subtypes can be distinguished: long-wavelength sensitive cones (L-cones) highly expressed known L-cone specific gene *OPN1LW*, known cone markers *ARR3* and *GUCA1C*, and novel markers including *TDRG1* and *MYL4*. Middle-wavelength cones (M-cones) highly expressed specific known gene *OPN1MW* and novel marker *AC023905.1*. The remaining expression patterns of L- and M-cones are very similar. The short-wavelength or blue cones (S-cones) highly expressed specific known marker *OPN1SW*, known cone marker *TTR*, and novel marker *CCDC136* and *CLTB* (Table S1 in Supporting Information). To validate the new marker gene *MYL4* for cones identified by scRNA-seq analysis, we performed an *in situ* hybridization experiment for the gene and confirmed the co-expression of *MYL4* with the known cone marker *ARR3* (Figure S2B in Supporting Information). High diversities of amacrines can be identified according to their morphologies (Kolb et al., 1992). Twelve amacrine subtypes were identified in this study by high expression of known markers for amacrine cells *GAD1* and *GAD2*, as well as distinguished expression markers (Figure S2B, D, Table S1 in Supporting Information). For bipolar cells, 14 subtypes could be identified through high expression of known markers *VSX2*, *VSX1*, *TRPM1*, and other markers (Figure S2C, D in Supporting Information). Of the 14 bipolar cell subtypes, nine can be identified as on-bipolar by the expression of *TRPM1*, and the remaining five are off-bipolars. To validate the new marker genes for bipolar subtypes discovered by scRNA-seq, we performed an *in situ* hybridization experiment for the genes *ERBB4*, *PCP2*, *CABP2*, *CXCL14*, *TPH1*, and *AC067969.1*, and confirmed that these new bipolar markers co-colalizated with known bipolar gene *VSX2* (Figure S2D–F in Supporting Information), further indicating these genes are new markers for bipolar cells. Six subtypes of horizontal cells were identified through high expression of known marker *ONECUT1*, as well as distinguished expression of known marker *ONECUT2*, and other markers (Figure S2B, D in Supporting Information). Sixteen RGC subtypes can be identified through high expression of known marker *NEFL*, as well as distinguished expressions of known marker *NEFH*, and other markers (Figure S2B, D, Table S1 in Supporting Information). For the non-neuronal cells in the

A

Donor	Age	Sex	Eye	Cause of death
1	E23rd weeks	Male	OS	Down's syndrome
2	P4th days	Male	OS	Skull malformations
3	7 years	Male	OS	Traumatic brain injury
4	21 years	Male	OS	Cerebral asphyxia
5	32 years	Male	OS	Traumatic brain injury
6	44 years	Male	OS	Brainstem hemorrhage
7	56 years	Male	OS	Severe toxemia
8	62 years	Male	OS	Carcinoma of trachea
9	81 years	Male	OS	Heart failure

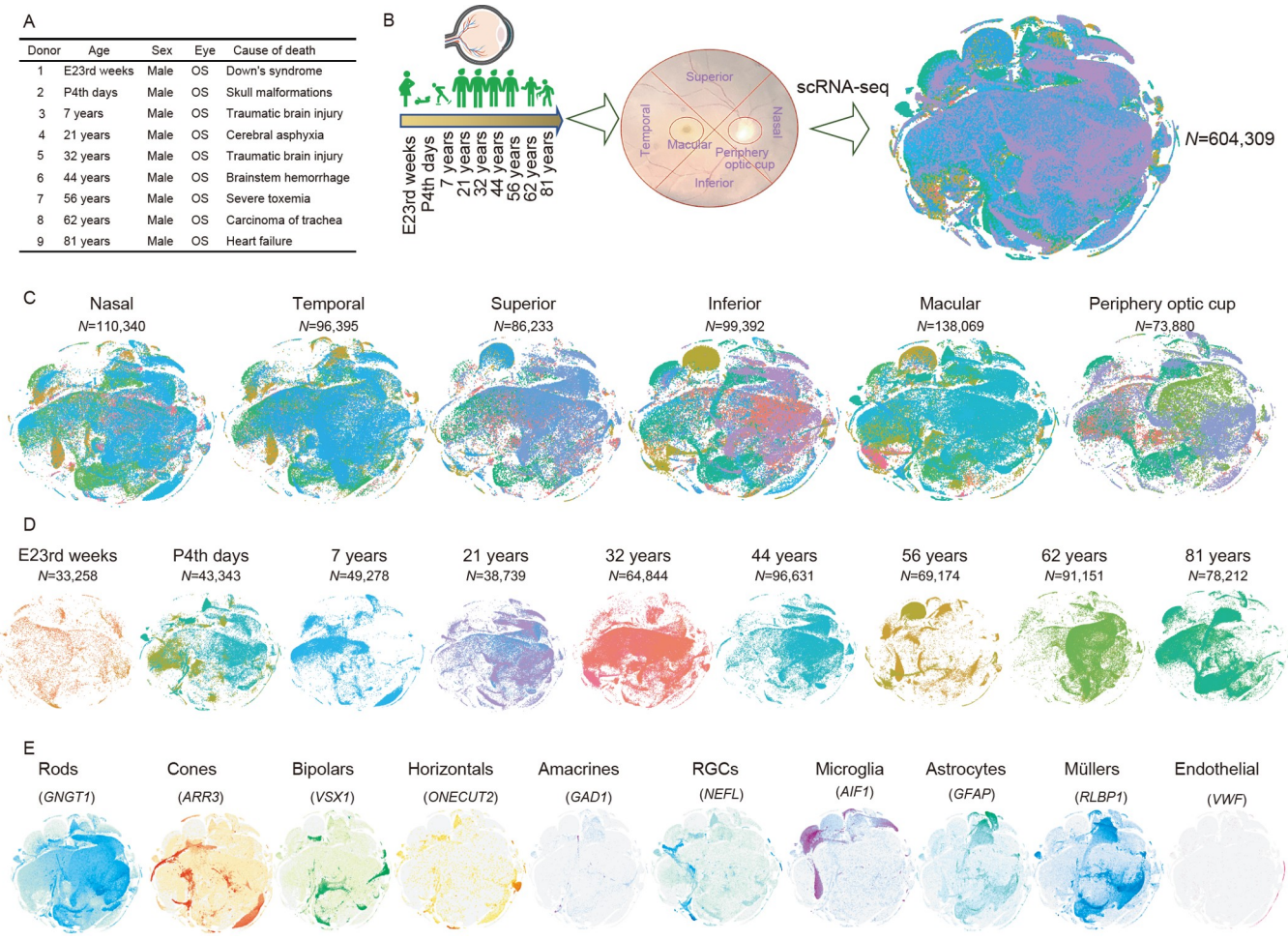

Figure 1 Single-cell RNA sequencing (scRNA-seq) of 609,304 cells from six human retina regions across nine ages. A, scRNA-seq donors' information. B, Workflow of the experimental scheme design and *t*-SNE visualization of 609,304 human retina cells. C, *t*-SNE visualization of cells from six human retina regions colored by samples. D, *t*-SNE visualization of cells from nine ages colored by samples. E, Annotated based on known marker genes of 10 main retina cell types.

human retina, two subtypes of Müller cells were identified by the differential expression of known marker *RLBP1* and novel markers (Figure S2G, Table S1 in Supporting Information). Two subtypes of astrocytes could be distinguished through the high expression of known marker *GFAP* and differential expression of other markers. Three microglia subtypes could be identified through the high expression of known markers *AIF1*, as well as distinguished expressions of *HLA-DRA* and other markers. In addition, one type of VECs can be identified by the known marker *VWF*, as mentioned above.

The regional cell proportion difference in the human retina

To investigate the proportion of the 10 cell types among the six retinal regions, we counted the number and calculated the proportion for each cell type in six regions. In all, the rods comprised about 50.1% of all retinal cells. The next highest percentage of cells is Müller glia, accounting for 22.73% of all the retinas. Microglia (10.34%), bipolar (7.50%), and cones (3.76%) come as the next populations. Astrocytes (2.06%), horizontals (0.99%), amacrines (0.19%), RGCs (2.06%), and VECs (0.27%) are small populations in the retina (Figure 2A). In the macula, higher retinal neuron proportions (cones, horizontals, bipolar, amacrines, and RGCs) were detected than in the rest of the regions, which is consistent with the sharpest vision acuity in the macular region. Consistently, astrocytes, which are usually present in the RGC layer and optic nerve, also showed a higher proportion in the macular region than in the rest of the regions. Two glia cells—Müller glia and microglia—showed much lower proportions in the macula compared to those in the other regions (Figure 2A). The bipolar cell proportion in the superior retina (6.87%) was higher than that of the inferior retina (3.38%). Similarly, there were more cones in the superior retina (4.45%) than in the inferior retina (3.78%). The distribution of RGCs in the inferior retina (2.70%) was almost twice that of the superior retina (1.35%) (Figure 2A). These results suggest that the human retina is a tissue with

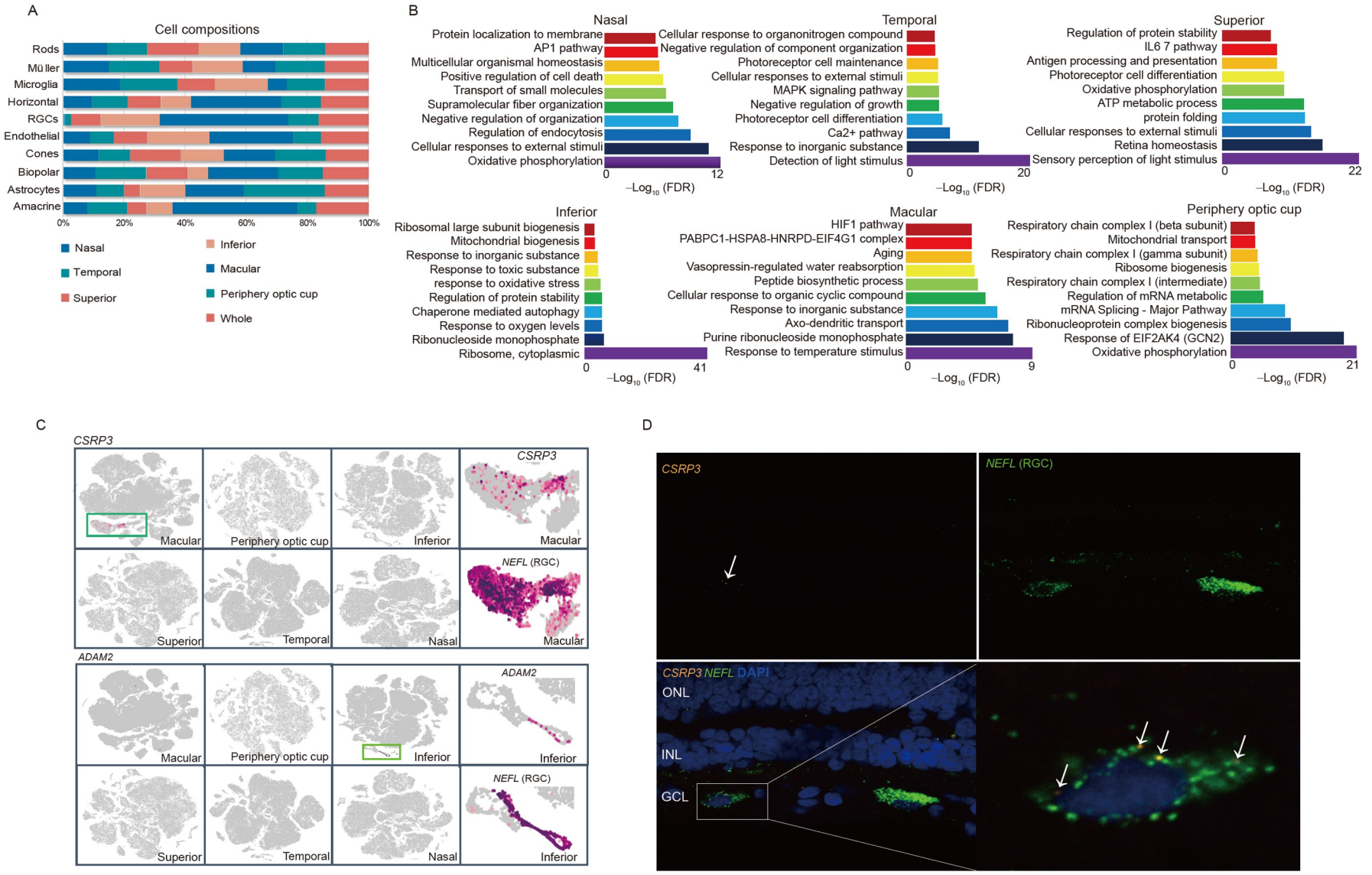

Figure 2 Regional preferred genes of the six human retinal regions. A, The cell percentage proposition of each of the 10 main cell types in six retinal regions. B, Top 10 functional annotations of the DEGs in each of the six human retinal regions. C, *t*-SNE visualization of *CSRP3* and *ADAM2*, which are expressed only in a specific region of the human retina. D, RNAscope RNA *in situ* hybridization expression of *CSRP3* and *NEFL* (RGC marker) in the macular region. *CSRP3* is expressed in some *NEFL* positive cells.

polarity. The differentially expressed genes (DEGs) among the regions reflect the spatial functional difference of the human retina (Figure 2B, Figure S3, Table S2 in Supporting Information). To explore the preferred expressing genes in each retinal region (only detected in the corresponding region), we compared the gene expression patterns in the six retinal regions (Figure 2C and D, Table S3 in Supporting Information). In total, 117, 329, 9, 94, 538, and 24 preferred expressing genes were detected in the nasal, temporal, superior, inferior, macular, and periphery optic cups, respectively (Table S3 in Supporting Information). Of these preferred genes, *CSRP3* was only expressed in RGCs of the macula (the first two panels in Figure 2C), as validated by RNA *in situ* hybridization (Figure 2D). Similarly, *ADAM2* was only expressed in RGCs of the inferior retina (Figure 2C, second panel). These regional preferred genes may contribute to the visual polarity (Nomura et al., 2005; Whitmore et al., 2014) of the human retina.

Cell compositions of different ages' retinas

We investigated the cell proportions at different ages in the human retina (Figure 3A). In general, the retinas of seniors contain fewer retinal neurons than those of children and adults, which is consistent with a previous study (Harman et al., 2000) (Figure 3A). The cell composition of the immature retina is different from that of the mature retina. The E23rd week's retina contains 18.41% immature rods (marked by *NRL*, but *RHO* and *CNGA1* are negative) (Figure S4A in Supporting Information). Neural progenitor cells account for 8.71% of all retinal cells. These cells highly expressed *TOP2A* (Isik et al., 2015), *CENPF* (Baffet et al., 2015), *AURKB* (Lian et al., 2019), and *UBE2C* (Vasiljevic et al., 2013). The proportion of VECs was very high (8.20%) at this stage. Two transitional cell types were detected at this time. Among them, one accounted for 4.44% of all cells and is involved in the HIF-1 signaling pathway, etc. (Figure S4B, first panel, in Supporting Information). The other accounted for 9.42% of all cells and highly expressed immune-related genes (Figure S4B, second panel, in Supporting Information). On the P4th day retina, all main cell types of the retina appeared. The mature cones appeared at this time with a high proportion (18.81%) (Figure 3A, Figure S4C in Supporting Information). Among them, L-cones accounted for 84.05%, M-cones for 12.75%, and S-cones for 3.2% (Figure S4D in Supporting Information). On the P4th day retina, a transitional cell type was detected (0.39%) (Figure S4E in Supporting Information). Transitional cell types may contribute to their specific developmental processes.

Retina gene expression dynamics with aging

To identify the age-dynamic changes of gene expression in the human retina, we grouped 21 years, 32 years, and 44 years as adults and used the ages of E23rd weeks, P4th days, 7 years, 56 years, 62 years, and 81 years to compare to the group of adults, respectively (Figure 3B). The number of DEGs was related to the cell type (Figure 3C, Figure S5A in Supporting Information). For example, the highest number of DEGs was found in rods (41%), followed by bipolar (20%), and Müllers (11%). Pairwise correlation heatmaps of DEGs at each age suggested the dynamic changes of each cell type (Figure S5B in Supporting Information). Compared to adults, E23rd weeks, P4th days, 7 years, 56 years, 62 years, and 81 years also had their preferred expressed genes (only expressed at the corresponding age) (Figure S5C, Table S4 in Supporting Information). The functions of DEGs at each age may reflect their visual characteristics (Figure S5D–E, Table S5 in Supporting Information).

We further calculated the correlations of gene expression with age (Figure S6, Table S6 in Supporting Information). The top negatively correlated genes (correlation=−0.65–−0.99) are involved in chromatin stability, including covalent chromatin modification (Figure 3D, E, upper panel; Figure S6, Table S6 in Supporting Information), chromatin remodeling, CtBP complex, regulation of chromatin organization, epigenetic regulation of gene expression, and chromatin assembly or disassembly. These results indicated that decreased stability of chromatin might be one of the main reasons for retinal senescence. On the other hand, the top positive correlated group is mitochondrion organization (correlation=0.65–0.99), which involved genes *QDPR*, *DNAJC19*, etc. (Figure 3D, second panel), are highly enriched in retinal neurons of cones, RGCs, horizontals, and amacrines (Figure 3E, first panel; Figure S6, Table S6 in Supporting Information). These results suggested that gene expression within the human retina undergoes profound dynamic changes during natural aging.

Highlighted DEGs with aging

Of the genes with dynamic expression across ages, HIF-1 signaling should be addressed because it showed a reverse parabola expression pattern across ages. The expression level of HIF is higher in children and seniors than in adults. HIF-1 signaling is strongly activated during retinal development (E23rd weeks and P4th days, represented by elevated *VEGFA* and *HIF1A*), and then tends to stabilizein adults (21, 32, and 44 years), which is consistent with previous reports (Zepeda-Romero et al., 2017) (Figure 4A, Figure S7A in Supporting Information). Interestingly, at 56 years, the expression of HIF-1 signaling-related genes began to increase, represented by *HIF1A*, *CDKN1A*, *CDKN1B*, etc. (Figure S7A in Supporting Information). At 62 years, the expression of *VEGFA* was enhanced in Müller glia and astrocytes (Figure 4C). At 81 years, the expression of *VEGFA* was enhanced extensively

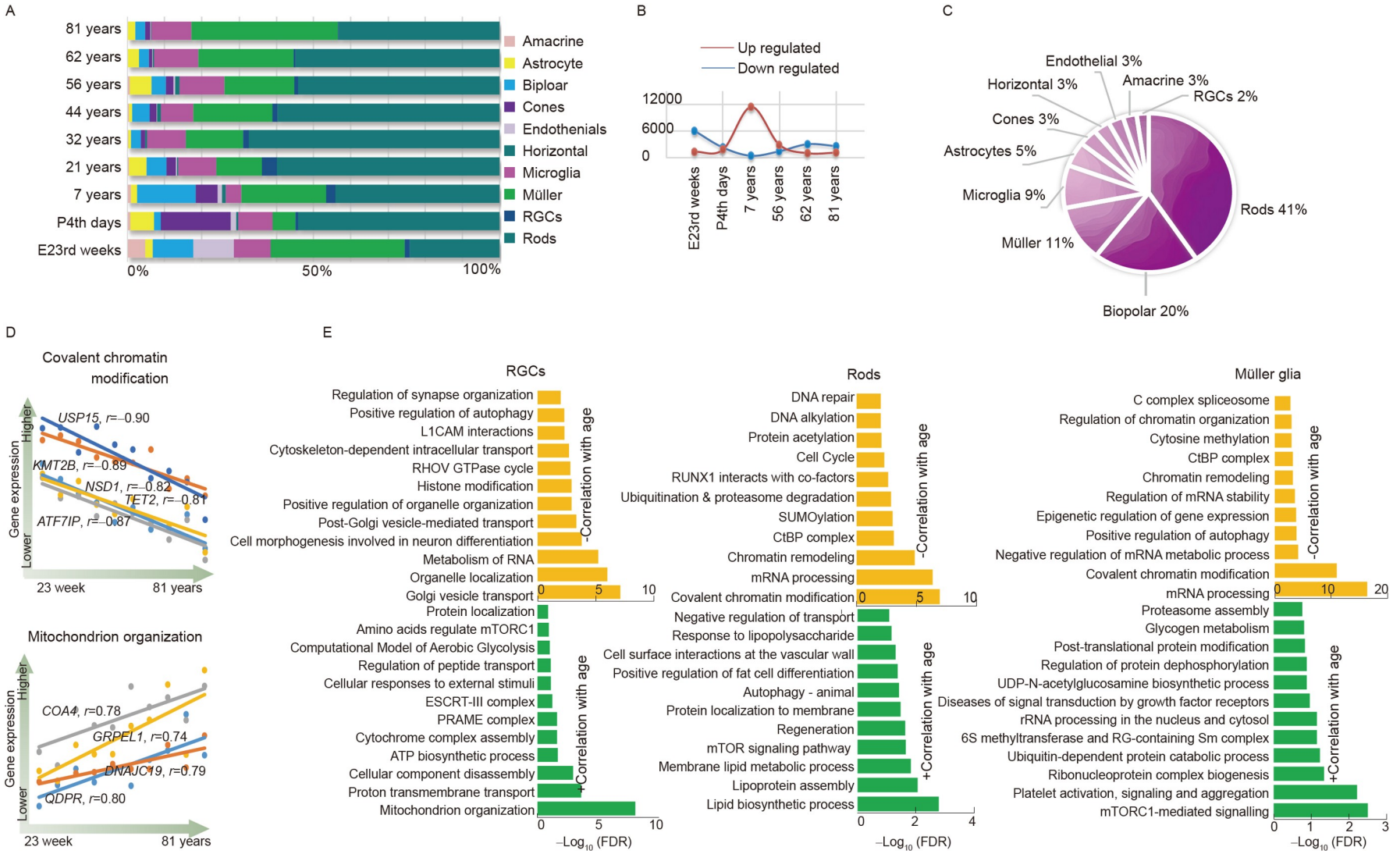

Figure 3 Cellular changes across ages. A, The cell percentage of each of the 10 main cell types across nine ages in graphical representation. B, The number of DEGs of E23rd weeks, P4th days, 7 years, 56 years, 62 years, and 81 years compared with the adult group (21 years, 32 years, and 44 years), respectively. C, The cell percentage of the number of DEGs. D, The most enriched negative correlation function (covalent chromatin modification, first panel) and the positive correlation function (mitochondrion organization) with age. E, The enriched function/pathways positive or negative correlated with age for RGCs, Rods, and Müller glia (all cell types correlation results are presented in Figure S6 in Supporting Information).

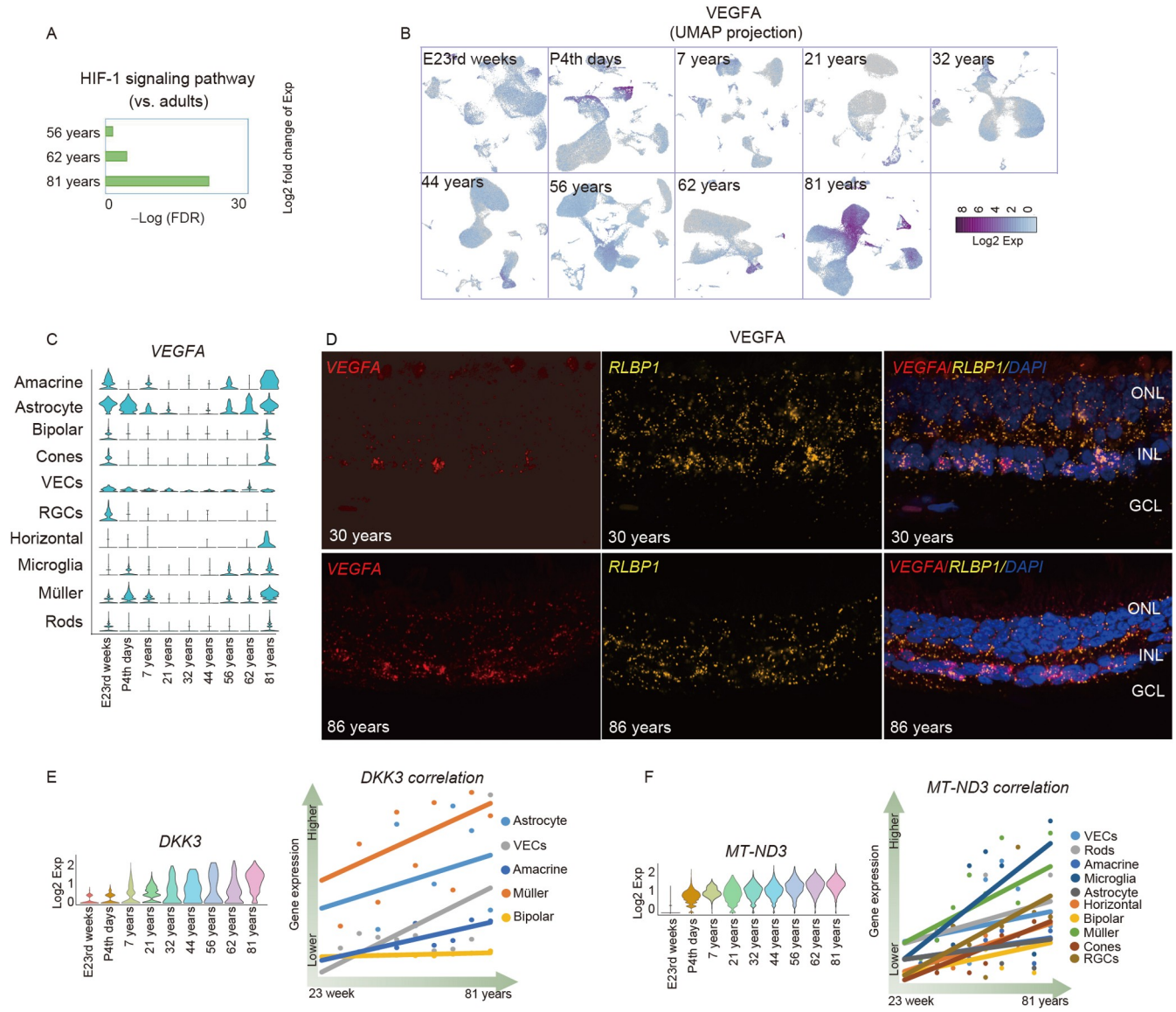

Figure 4 Highlighted genes' increased expression in aging retinas. A, Enriched HIF-1 signaling pathway-related genes at different ages compared to the adult groups (21, 32, and 44 years). B, UMAP visualization of *VEGFA* in individuals across nine ages. *VEGFA* is widely expressed in 81-year-old individuals. C, The violin plots of *VEGFA* expression in each cell and each age. D, The RNA expression pattern of *VEGFA* was confirmed by RNAscope *in situ* hybridization experiments at adult age (30 years) and old age (86 years) (Müllers marked by *RLBP1*). *VEGFA* is widely expressed in seven-year-old individual. ONL, outer nuclear layer; INL, inner nuclear layer; GCL, ganglion cell layer. E, The violin plots of *DKK3* expression in each age (left panel) and the correlation of DKK3 expression and ages in five retina cell types (right panel), suggesting its strong positive correlation with age. F, The violin plots of *MT-ND3* expression in each age (left panel) and the correlation of *MT-ND3* expression and ages in 10 retina cell types (right panel), suggesting its strong positive correlation with age.

in microglia, Müller, astrocytes, rods, and bipolar cells (Figure 4B, C). The higher expression of *VEGFA* in the old retina was confirmed through RNA *in situ* hybridization (Figure 4D). It is speculated that the increased *VEGFA* level in seniors may be involved in aging-related retinal angiopathy, such as wet age-related macular degeneration (wet AMD) (Deng et al., 2022; Huang et al., 2016), neovascular glaucoma (Huang et al., 2019; Liao et al., 2016), etc.

Through correlation analysis of gene expression with age, we also noted the upregulation of mitochondrial function-related genes. *DKK3*, which is involved in mitochondrial function (Yang et al., 2012; Zhou et al., 2017), is significantly upregulated with aging (Figure 4E). *MT-ND3*, which encodes mitochondrially NADH: ubiquinone oxidoreductase core subunit 3, is also upregulated with age (Figure 4F). On the other hand, some other mitochondrial oxidative phosphorylation-related genes (Kummer and Ban, 2021) such as *MT-ATP6* and *MT-CO1* showed lower expression in the early development period (E23rd weeks or P4th days) and higher expression after 40 (44, 56, 62, and 81 years) than in the middle or young ages (7, 21, and 32 years) (Figure S7B in Supporting Information). The high expression of

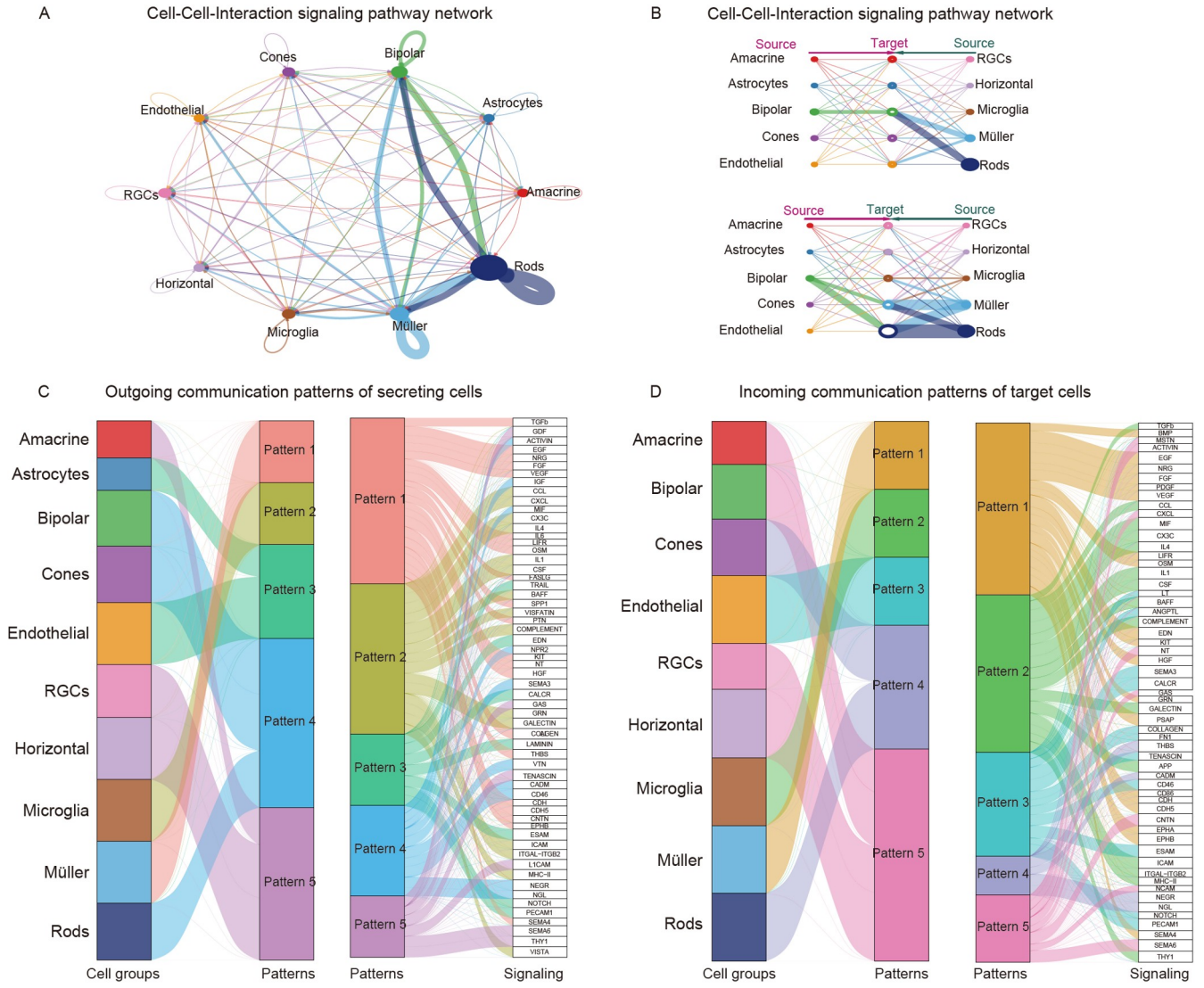

Figure 5 Cell-cell interaction in 10 main cell types of the human retina. A, Circle visualization for human retina cellular communication among the 10 main cell types, predicted by CellChat. B, Hierarchy visualization for human retina cellular communication among the 10 main cell types, predicted by CellChat. C, The alluvial plot shows outgoing communication patterns of secreting cells among the main human retina cell types. D, Incoming communication patterns of target cells among the human retina's main cell types.

these genes may result from the mitochondrial stress response from aging (Correia-Melo et al., 2016; Li et al., 2020). These results might imply that the mitochondria function in the retina start to show signs of ageing in our 40s.

Immune-related genes mainly expressed in microglia were enhanced with aging (Figure S8A in Supporting Information). In the aged retina, *CXCL8*, *HLA-DQB1*, and *HLA-DRB1* were significantly upregulated (Figure S8B in Supporting Information). At the age of 81, a higher proportion of microglia cells marked by high expression of *S100A8* and *S100A9* appeared (Figure S8C, D in Supporting Information). The function of microglia-3 mainly involves myeloid leukocyte activation. As for aging, this result suggested that activation of immune cells is especially actived (Stephenson et al., 2018; Yaqoob, 2017).

Cell-cell interaction in the human retina

The molecular connections between retinal neurons and glial cells are poorly understood in the retina. To address this question, we analyzed the retinal cell-cell communications using CellChat (Jin et al., 2021). We detected 256 significant ligand-receptor pairs among the 10 main cell types, which were further categorized into 78 signaling pathways, including TGFβ, VEGF, COMPLEMENT, etc. (Figure 5 and Figure S9, Table S7 in Supporting Information). A systematic network for cell-cell communication of 10 retina main cell types is shown in Figure S5A and B in Supporting Information. Multiple cell groups and signaling pathways coordinated with function analysis uncovered five patterns for outgoing signaling (Figure 5C) and five for incoming

signaling in the human retina (Figure 5D). These results show that (1) two distinct retinal neuron cell types in human retinas may connect through hoverlapping signaling networks, and that (2) certain cell types, such as Müller cells and microglia, simultaneously activate multiple signaling patterns and pathways, whereas other cell types, such as photoreceptors, exhibit fewer and more homogeneous communication patterns.

The application of functional similarity grouping identified four groups of pathways (Figure S10A in Supporting Information). For example, group 1 is dominated by vascular homeostasis pathways (e.g., TGFβ, VEGF) and largely represents autocrine signaling from Müllers and VECs. For the VEGF signaling pathway sender, both the receiver and mediator are Müller cells, and they influence almost all cell types (Figure S10B, upper panel, in Supporting Information). This signal transduction is mainly through the VEGFA and VEGFB pathways (Figure S10B, lower panel, in Supporting Information). With each age analysis, the Cellchat results also suggested that human retina cell-cell communication has a certain dynamic change with aging (Figure S10C in Supporting Information).

Transcriptional regulation in the human retina

A regulon is a collection of genes or operons under the regulation of the same regulatory protein (Novichkov et al., 2010). Through SCENIC regulatory network analysis (Aibar et al., 2017), a total of 158 regulons were detected in human retinal cells across different ages (Figure S11, Table S8 in Supporting Information). In regulon BCLAF1, the most enriched target genes (1,348, the number of target genes in this regulon and the same below) were detected, followed by POLR2A (1,048), ELF1 (1,015), and IRF1 (1,005). Some of these 158 regulons showed cell-type specificity. For example, regulons SOX5 (114), NFE2L1 (406), and IRX2 (21) are relatively highly expressed in RGCs. In summary, the VECs and microglia showed some degree of similar transcriptional regulation patterns, while Müllers and astrocytes showed some degree of similar expression patterns (Figure S11A in Supporting Information). Two of the four Yamanaka transcription factors (TFs) related regulons SOX2 and MYC (Takahashi and Yamanaka, 2006) were mainly enriched in the VECs and Müllers, respectively. The expression patterns of each regulon are dynamically changed across different ages (Figure S11B in Supporting Information), suggesting that gene expression is regulated consistently with age. In all, each age had its enriched regulons. For example, at 81 years, the HMGB2 regulon was highlighted. *HMGB2* encodes a non-histone chromosomal high mobility protein that can bend DNA and enhance its flexibility to promote TF binding (Fan et al., 2002; Ugrinova et al., 2009). *HMGB2* may act in a redox-sensitive manner (Zhao et al., 2020). These results may suggest that the stability of chromatin also decreases in old age in a non-histone manner, which is consistent with the above-age correlation results.

DKK3 as a regulator for retinal mitochondria senescence

Previous evidence has suggested that mitochondria plays a central role in aging-related neurodegenerative diseases (Lin and Beal, 2006). *DKK3*, which overexpression can induce cell apoptosis through the mitochondrial pathway (Yang et al., 2012; Zhou et al., 2017), is up-regulated with human aging retina in the above results. Therefore, we investigated the relationship between *DKK3* and mitochondrial function. *DKK3* overexpression in 293T cells decreased mitochondrial membrane potential (MMP). On the contrary, *DKK3* shRNA knockdown increased MMP (Figure 6A, first panel, B). The irregular, dilated, circular abnormal morphology of $NaIO_3$-induced mitochondria can be rescued by *DKK3* shRNA knockdown, but not by *DKK3* overexpression (Figure 6A, second panel). Transmission electron microscopy (TEM) results validated that *DKK3* overexpression enhanced the $NaIO_3$-induced mitochondrial abnormality, which showed partial swelling and partial dissolution of mitochondrial cristae, and reduction of electron density (Figure 6C, second panel; Figure 6D, upper panel). The $NaIO_3$-induced mitochondrial abnormality can be partially rescued with *DKK3* shRNA knockdown (Figure 6C, third panel; Figure 6D, lower panel). Taken together, *DKK3* overexpression can damage mitochondrial morphology and reduce MMP in 293T cells. We further tested the reactive oxygen species (ROS) in 293T and found *DKK3* overexpression can reduce ROS during $NaIO_3$ treatment (Figure S12A, B in Supporting Information), suggesting that *DKK3* overexpression can reduce ROS under $NaIO_3$ treatment.

To further clarify the effect of *DKK3* on mitochondria *in vivo*, we injected *DKK3* overexpressing AAV virus into the vitreous (1 μL per vitreous body with virus titer 3×10^{13} vg mL^{-1}) of 18-month-old mice (old mice). Through TEM analysis three months after injection of *DKK3* overexpressed AAV, the photoreceptor layer was observed with disordered, shorter, smaller, and highly disordered mitochondrial structures compared to the GFP AAV control group (Figure 7A, left two panels). In addition, in the RGC layer cells (Figure 7B, left two panels), swelling, and vacuolation of mitochondria and abnormal mitochondrial cristae were observed. Smaller and abnormal mitochondria can also be observed widely distributed in the *DKK3* overexpression optic nerve compared to the GFP control group (Figure 7C, left two panels). We also injected *DKK3* knockdown AAV into the vitreous of old mice and found that, compared with the control group, *DKK3* knockdown presented different degrees of abnormalities in the mitochondrial morphology of these cells (Figure 7A–C, right two panels). These results

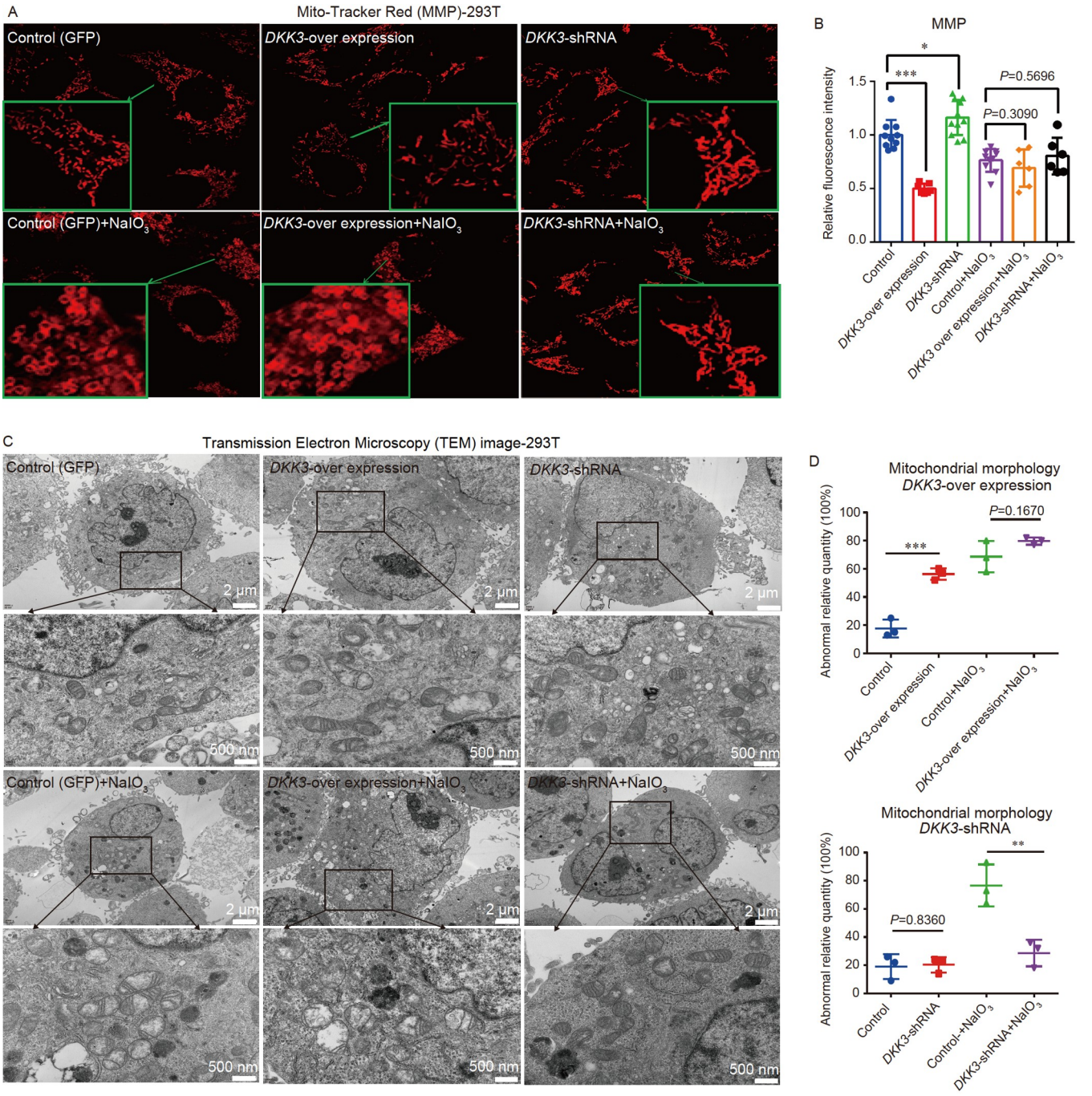

Figure 6 Effects of *DKK3* on mitochondrial function in HEK-293T cells. A, Representative confocal images of mitochondrial morphology (stained by Mito-Tracker Red CMXRos) and mitochondrial membrane potential (MMP). The region bounded by the box is shown as an enlarged region for each experimental condition. Scale bars, 20 μm. B, Quantification analysis of the images of MMP in each treatment. Numbered data points represent individual mitochondria manually traced. C, TEM analysis of the mitochondrial structure in each treatment. The region bounded by the box is shown as an enlarged region for each experimental condition. D, Quantification of percent abnormal mitochondria in cells treated with or without $NaIO_3$ (20 mg mL^{-1}).

suggest that when the expression of *DKK3* is too high or too low, mitochondrial abnormalities may occur in the retina.

To further investigate the effect of *DKK3* overexpression on the morphology of retinal cells, we stained the retina with different cell markers (Figure 8, Figures S13–S15 in Supporting Information). The *DKK3* protein immunofluorescence staining after *DKK3* AAV overexpression (Figure 8A, left two panels) and *DKK3* shRNA AAV knockdown (Figure 8A, right two panels) indicated the expression levels of *DKK3*. We performed immunohistochemical staining on markers of retina cell types, including rods (Rho antibody), cones (Arr3 antibody), RGCs (Brn3a), microglia (Iba1 antibody), and Müller glia (Rlbp1 antibody). These results suggested thatthe expression of Rho

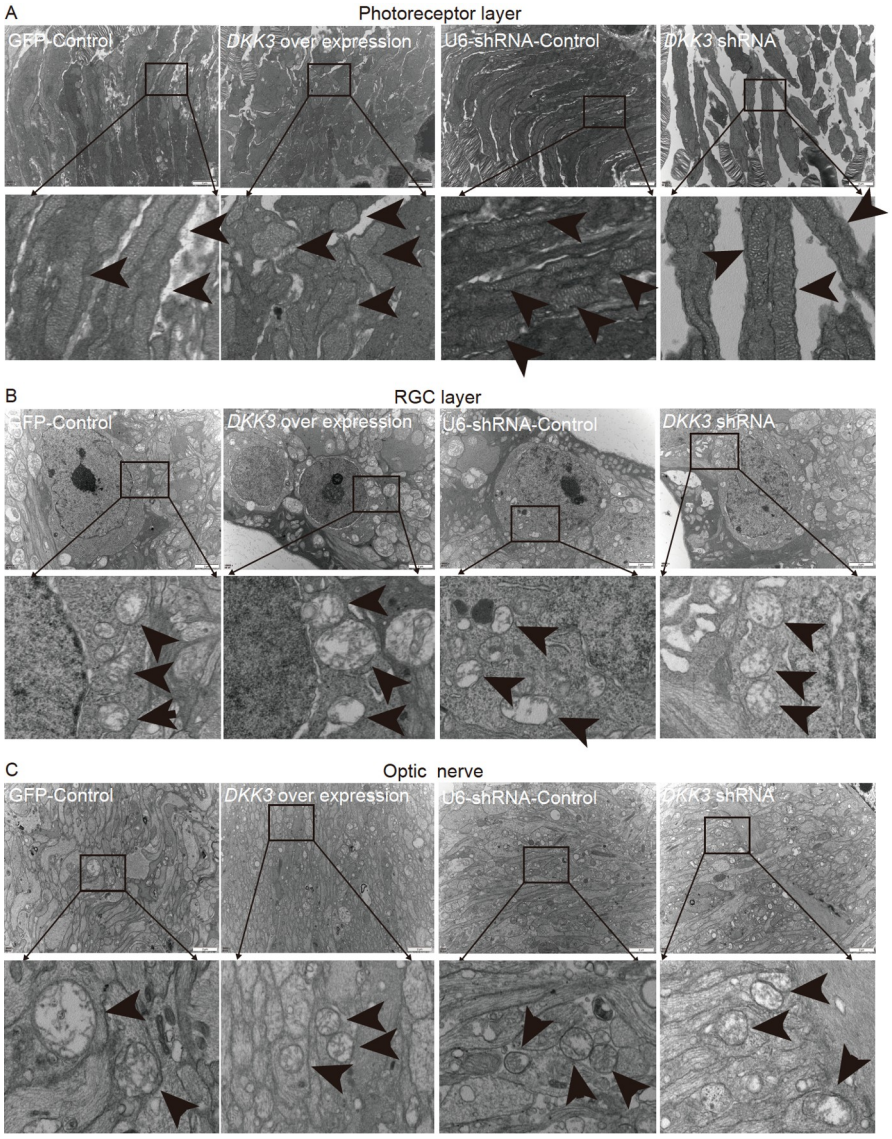

Figure 7 TEM analysis of effects of *DKK3* in the mice retina. TEM analysis of mitochondrial structures in old mice (18 months) retina of photoreceptor layer (A), RGC layer (B), and optic nerve (C). The region bounded by the box is shown as an enlarged region for each experimental condition.

in the outer segment in the retina of oldmice was weaker in *DKK3* overexpression group than in the control group (Figure 8B, the left two panels of the first row, Figure S14A in Supporting Information). In the young mice, the cone morphology of *DKK3* overexpression was similar to that of the old mice (Figure 8C). *DKK3* overexpression increased Brn3a positive RGCs (Figure 8D, the second row, as shown by the arrow, Figure S15B in Supporting Information). In old mice, the number of microglia in *DKK3* overexpression group was significantly less than that in the control group (Figure 8E, the first row). *DKK3* expression has no obvious effect on Müller glia (Figure S15 in Supporting Information). TUNEL cell apoptosis detection suggested no signals for either *DKK3* overexpression or *DKK3* knockdown in the mice retina (Figures S13, S15 in Supporting Information). These results suggested that *DKK3* overexpression had an impact on the aging retina, and its mechanism needs to be further investigated.

DISCUSSION

Due to the difficulty of obtaining critical human tissues, such as the retina, it has been challenging to determine the deep molecular events underlying the human vision system. Here, we sequenced the RNA of over 0.6 million single cells from human retinas across six regions at nine ages. The primary discoveries in the current study included the following: (1) at least 60 retina cell subtypes were identified (six horizontal, 14 bipolar, 12 amacrine, 16 RGC, three cone, one rod cell, two astrocyte, three microglia, two Müller, and one endothelial cell subtype); (2) the elevation of the *VEGFA* with aging

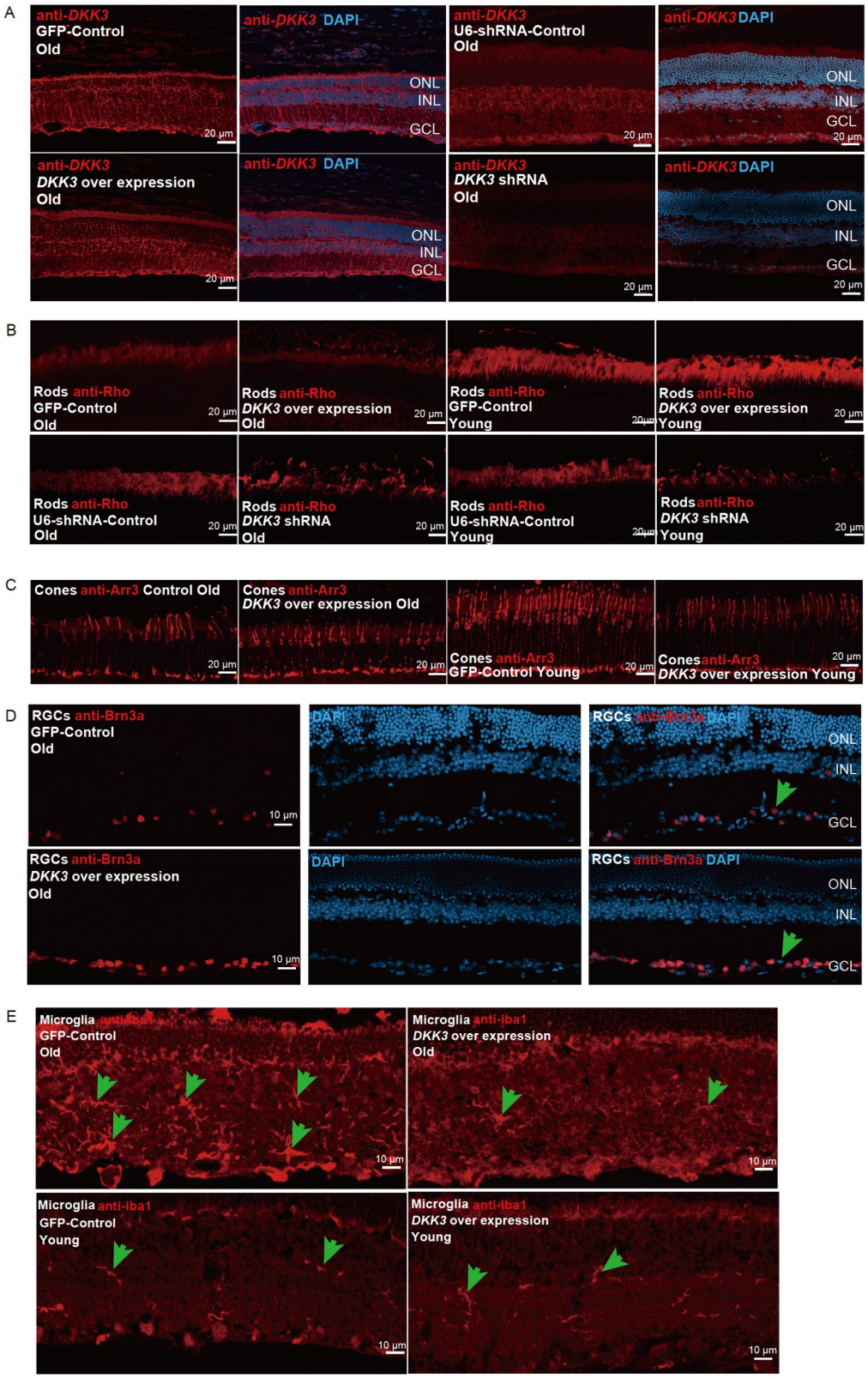

Figure 8 Effects of *DKK3* in mice retina. A, Immunofluorescence staining of *DKK3* in old mice retina with *DKK3* overexpression or knockdown. B, Immunofluorescence staining of Rho, which labeled rods with *DKK3* overexpression (first row) or *DKK3* knockdown (second row) in old and young mice (2 months). C, Immunofluorescence staining of ARR3, which labeled cones with *DKK3* overexpression in old or young mice. D, Immunofluorescence staining of Brn3a, which labeled RGCs with *DKK3* overexpression in old mice. E, Immunofluorescence staining of Iba1, which labeled microglia with *DKK3* overexpression in old or young mice. ONL, outer nuclear layer; INL, inner nuclear layer; GCL, ganglion cell layer. The arrows indicate some microglia. More results related to this figure are presented in Figures S13 and S15 in Supporting Information.

should promote the pathological neovascularization in the human aged retina in disease conditions such as wet AMD ordiabetes retinopathy (DR); and (3) our analysis also revealed *DKK3* overexpression impacted the mitochondrial homeostasis, which may promote retinal senescence.

Illumination of different regions of the human retina elicits differences when exposed to equal illuminance of light, suggesting that the light response of different regions of the retina are not equal (Szél et al., 2000). Previous studies focused on the distribution of retinal neurons in peripheral and macular regions (Kolb et al., 2020). However, there are few studies concerning the cell compositions of other specific regions of the human retina, such as superior, inferior, nasal, or temporal. A bulk RNA sequencing analysis illustrated the region-associated molecular alteration in human retinas (Whitmore et al., 2014). However, due to the heterogeneity of retina cell types, the bulk-seq results might not reveal changes among cell types. By using scRNA-seq, most of the previous studies only focused on the differences between macular and peripheral retinas (Lu et al., 2020; Peng et al., 2019). Here, we present the first scRNA-Seq dataset to separately investigate the cellular composition and molecular mechanisms in the superior, inferior, nasal, temporal, macula, and peripheral optic nerve regions of the human retina.

Neurons are highly diverse in the retinas of different species (Masland, 2001). Due to different observation methods, the retinal cell subtypes may not be exactly the same, but the main cell types are similar among species. In the 20th century, the mammalian retina consisted of >60 distinct types of neurons, identified mostly by Golgi staining and electron microscopy technology, each playing a specific role in processing visual images (Masland, 2012). In 1992, through Golgi staining, three horizontal cell types, 27 amacrine cell types, nine bipolar cell types, and 18 RGC types were identified in the human retina (Kolb et al., 1992; Masland, 2001). In recent years, mammalian retina cell types have been identified based on gene expression levels of scRNA-seq analysis, with 39 cell types identified in mice retina (Macosko et al., 2015) and >65 cell types in macaque retina (Peng et al., 2019). Unlike Golgi staining and electron microscopy technology, scRNA-seq based on gene expression largely relies on sequenced cell numbers and their diversity to identify cell types. Although cell subtypes were identified in the mice and macaque retinas based on scRNA-seq, previous studies on scRNA-seq of the human retina mostly focused only on the gene expression patterns of the 10 main cell types because of limited sequenced cells rather than identifying the cell subtypes (Hu et al., 2019; Lu et al., 2020; Lukowski et al., 2019). In this study, we sequenced over 60 million human retinal single cells and identified 60 cell subtypes in the human retina. When comparing humans to macaques, the same types of rods (one type), and cones (three types: L-, M-, and S-) were identified (Peng et al., 2019). We also identified 12 subtypes of amacrine cells in humans and 34 subtypes in the macaque. Extreme diversity among amacrine cells was observed in nonhuman vertebrates (MacNeil and Masland, 1998). In the rabbit, 29 subtypes of amacrines were identified through morphological observation with Golgi staining (Macneil et al., 1999). For bipolar cells, 14 subtypes were identified in humans and 12 in the macaque. For horizontal cells, we identified six horizontal cell subtypes in humans and two in the macaque (Peng et al., 2019). For RGCs, we identified 16 RGC subtypes in humans and 18 in the macaque. In this study, we could not link the morphology and function of each cell subtype of human retinal neurons, which could be a direction for further research.

Because of limited material availability, few studies concerning the cell compositions of developmental, adult, and aged retinas have been reported, particularly for human retinas (Shen et al., 2020). Most of the previous studies detailed evolutionarily conserved and specific mechanisms controlling the development of mammal retina (Clark et al., 2019; Cowan et al., 2020; Lu et al., 2020), but the molecular mechanisms underlying human retina aging remain largely unknown. A recent scRNA-seq analysis revealed that oxidative stress is a major aging feature of the cells in the neural retinal layer of monkeys (Wang et al., 2021b). However, due to the heterogeneity of lifestyles between monkeys and human beings, the results might not reveal whether these changes were intrinsic molecular changes or simply reflected changes in the corresponding species. By using scRNA-seq in large cell numbers, we delineated comprehensive cell-type and age-associated gene expression changes in human retinas.

This study also has some limitations. Because human retina samples are difficult to obtain, the number of samples used in this paper is limited. Some quantitative analyses may not have sufficient statistical analysis effects based on limited samples.

In summary, this study provides a comprehensive single-cell transcriptomic atlas of human retinas from six regions at nine ages and broadens our understanding of cell identities and cell type-specific gene signatures in the human retina. Importantly, it offers insights into the cell compositions and molecular mechanisms underlying the retina region and aging in humans. This knowledge should be useful for basic research of retinal diseases.

MATERIALS AND METHODS

Experimental procedures

Primary human retina tissue samples scRNA sequencing

The collection of donor samples was approved by the Human Research Ethics Committee of the Sichuan Academy of Medical Sciences and Sichuan Provincial People's Hospital

(2019-327) and carried out following the approved guidelines. Informed consent was obtained from all donors or their clients, and the experiments conformed to the principles set out in the *Procedures and regulations for organ donation after the death of Chinese citizens* (2019 edition). Donors with eye disease were excluded from this study. For scRNA-seq, postmortem eye globes were collected by the ophthalmologist for donor cornea transplantation. The remaining eye globes were used for dissection to extract the retina. The lens, iris, and vitreous were removed gently. Following extraction, the retinal samples were dissected into six regions (including macular area-5 mm diameter of the fovea, the periphery of optic cup region-5 mm diameter around the optic nerve (not included optic nerve), superior retina-all the 90-degree angle tissue of superior region, inferior retina-all the 90-degree angle tissue of inferior region, nasal retina-all the 90-degree angle tissue of nasal region, and temporal retina-all the 90-degree angle tissue of temporal region). The choroid/RPE layers were excluded from the sample collection. The retinal samples were then dissociated and processed for scRNA-seq using the 10X genomics platform right away. In total, 54 tissue samples from nine donors were used for sc-RNA sequencing.

Then, the segregated retinal sample was cut into small pieces in pre-cooled Dulbecco's phosphate buffered saline (DPBS) and washed three times with pre-cooled DPBS. The washed pieces were transferred to the preheated papain (2 mg mL^{-1}, Sigma) or mixed enzyme (trypsin and collagenase, Miltenyi Biotec, #130-095-929) and shook in the metal bath at 37°C for 10–40 min (350×*g*). When the tissue was loose and transparent, 5 mL DMEM+10% FBS was added to terminate the digestion. Then, the cells were transferred to pass the 70 μm mesh. 5 mL DMEM was added to wash the mesh. After that, centrifugation was performed at 4°C, 350×*g*, for 7 min. Then, the supernatant was removed and 100 μL DMEM+10% FBS was added to resuspend the cells. To count the cells, 10 μL cell suspension was added with 10 μL trypan blue and counted on the blood cell counting plate. If there were impurities, DMEM was used to supplement the suspension to 500 μL. Then, 250 μL Ficoll (Lymphoprep^{TM}) was added and centrifuged at 4°C, 800×*g*, for 20 min. The first and third layers of the cells were aspirated and transferred to a 15 mL centrifuge tube. As much DMEM as possible was added into the centrifuge tube and was centrifuged for 10 min at 800×*g* at 4°C, and the supernatant was discarded. 60–100 μL of pre-cooled DMEM +10% FBS was added into the centrifuge tube, and the cells were re-suspended and counted.

Cellular suspensions (about 8,000 cells per lane) were loaded on a 10X Genomics Chromium Single-Cell instrument to generate single-cell Gel Beads in Emulsion (GEMs). Single-cell RNA-seq libraries were prepared using Chromium Single-Cell 3′ Reagent Kits v3 according to the manufacturer's manual (CG000183 Rev C) for all samples. Reverse transcription of GEMs was performed in a Veriti Fast 96W Thermal Cycler-PCR (Thermo Fisher) with a semi-skirted 96-well plate (Eppendorf, #0030 128.605): 53°C for 45 min, 85°C for 5 min, held at 4°C. After reverse transcription, the GEMs emulsion was broken, and the single-stranded cDNA was cleaned up with DynaBeads MyOne Silane Beads (Life Technologies, #37002D). cDNA was amplified using a Veriti Fast 96W Thermal Cycler-PCR (Thermo Fisher) with 0.2 mL 8-strip non-flex PCR tubes with flat caps (STARLAB, #I1402-3700) at 98°C for three min, then 98°C for 15 s, 63°C for 15 s, 72°C for 1 min, cycled 11 times, then, 72°C for 1 min, held at 4°C. The amplified cDNA product was cleaned up with the SPRIselect Reagent Kit (Beckman Coulter, #B23318). Indexed sequencing libraries (Chromium i7 Multiplex Kit) were constructed using the reagents in the appropriate Chromium Single-Cell library kit v3 according to their user guide (10X Genomics), following these steps: (1) fragmentation, end-repair, and A-tailing, (2) post-fragmentation, end-repair, and A-tailing double-sided size selection–SPRIselect, (3) adaptor ligation, (4) post-ligation cleanup–SPRIselect, (5) sample index PCR, (6) post-sample index PCR double-sided size selection–SPRIselect, (7) post-library construction quality control (Bioanalyzer 2100, Agilent, USA). Then, each library was diluted to 2 nmol L^{-1}, and equal volumes of 16 libraries were pooled for each NovaSeq (Illumina) sequencing platform. The PE150 sequencing mode was adopted for about 30k read pairs $cell^{-1}$.

In situ RNA hybridization and quantification

Two eyeballs from the left eye of donors aged 30 years (cause of death: accidental injury) and 86 years (cause of death: lung cancer), and 12 samples from two donors were used for *in situ* hybridization experiments. The eyes' positions were marked with lines, fixed in 4% paraformaldehyde in PBS for 4 h, and transferred to 30% sucrose until they settled to the bottom of a tube. They were then embedded in OCT and processed for cryosection. *In situ* RNA hybridization was performed using the Advanced Cell Diagnostics RNAscope Multiplex Fluorescent Detection kit v2 (ACD, #323100) according to the manufacturer's instructions, following these steps: (1) prepare fresh frozen tissue sections, (2) fix the sections, (3) dehydrate the sections, (4) create a hydrophobic barrier, (5) apply RNAscope® hydrogen peroxide, (6) apply protease IV, and (7) proceed immediately to the RNAscope® Assay.

For multiplex staining, the following probes were used: *AC067969.1* (*Hs*-AC067969.1 1002381-C3), *AIF1* (*Hs*-AIF1 433121-C3), *ARR3* (*Hs*-ARR3 486461-C2), *CABP2* (*Hs*-CABP2 1000641-C3), *CD31* (*Hs*-CD31 548451), *CFH* (*Hs*-CFH 428731-C3), *CSRP3* (*Hs*-CSRP3 1000651-C2), *CXCL14* (*Hs*-CXCL14 425291-C3), *ERBB4* (*Hs*-ERBB4

407831-C1), *FCN1* (*Hs*-FCN1 831721-C2), *GPR37* (*Hs*-GPR37 513631), *HTRA1* (*Hs*-HTRA1 560621-C2), *MYL4* (*Hs*-MYL4 1001001-C1), *NEFL* (*Hs*-NEFL 468671), *PCP2* (*Hs*-PCP2 498161-C3), *RLBP1* (*Hs*-RLBP1 414221-C2), *S100A8* (*Hs*-S100A8 425271), *TPH1* (*Hs*-TPH1 310691-C3), *TRPM1* (*Hs*-TRPM1 816061), *VEGFA* (*Hs*-VEGFA 423161-C3), and *VSX2* (*Hs*-VSX2 493031-C2). Slides were counterstained with Prolong gold antifade reagent with DAPI (P36931, Life Technologies). The mounted slides were imaged on a ZEISS LSM900 fluorescent microscope (Carl Zeiss AG).

AAV vectors

For mouse *DKK3* overexpression, a pAV-CMV-P2A-GFP (NM_001360257.1) vector plasmid was constructed and packaged in AAV DJ. CMV starts the *DKK3*, Kozak sequence gccacc is added before the target gene ATG, the flag label is added at the C end of the target gene, and the target gene and GFP are expressed through P2a non-fusion. For overexpression control, only GFP and mCherry were expressed. For *DKK3* knockdown, eight shRNA sequences were constructed in pAV-shRNA-CMV-GFP vector and transfected in HEK 293 cells for knockdown efficiency tests. Finally, sequence 5′ CCAGGAAGTTCACAAGATATTCAAGAGATATCTTGTGAACTTCCTGGTTTTTT 3′, which showed 83% knockdown efficiency, was used and packaged in AAV DJ. For *DKK3* knockdown control, pAV-U6-shRNA-CMV-GFP was used. The final concentration of virus was 3×10^{13} viral genomes mL^{-1} in balanced salt solution (BSS) (Alcon, Forth Worth Texas) supplemented with 0.014% tween 20.

Cell culture and chemicals

HEK-293T cells were cultured in DMEM high glucose medium (GIBCO, USA) containing 10% FBS and 1% streptomycin. The cells were cultured in a moist 37°C constant temperature incubator. $NaIO_3$ (Solar Bio, China) was dissolved in 1×PBS and filtered by a 0.22 μmol L^{-1} filter membrane, configured as a 100 mmol L^{-1} storage solution. Before experimental use, $NaIO_3$ was diluted to 3 mmol L^{-1} by DMEM medium as a working solution.

AAV virus infection

HEK-293T cells were laid in an 8-chamber (0.17 mm glass-bottom plates, Cellvis, USA). When the cell confluence reached about 10%, the fresh medium was replaced and the AAV virus added (for the *DKK3* shRNA, the negative control was U6 nonsense siRNA; for the DKK overexpression virus, the negative control was GFP; the multiplicity of infection (MOI)=10^5). After 24 h of virus infection, the fresh medium was replaced, and the culture continued for 24 h. $NaIO_3$ was added 48 h after virus infection, and PBS was used as a negative control. Twenty-four hours after chemical treatment, the cells were collected for observation.

Living cell mitochondrial imaging

Live cell mitochondrial imaging was performed after 24 h of $NaIO_3$ treatment. Cells in *DKK3* knockdown and overexpression groups were stained with Mito tracker red cmxros (200 nm, beyotime, China). After the cells were incubated in a 37°C incubator for 15 min without light, the fresh medium was changed, and the mitochondrial morphology was photographed with a 63-fold oil microscope using laser confocal (LSM 800, Zeiss, Jena, Germany). The mitochondrial membrane potential can be expressed by analyzing the fluorescence intensity using Zen 2.1 software: "spline contour" in Zen 2.1 software is used to count the total mitochondrial fluorescence intensity in each cell in the photo to display the mitochondrial membrane potential intensity.

Mitochondrial ROS detection

After $NaIO_3$ treatment for 24 h, the cell mitochondrial ROS was detected. Mitosox was used in the cells of the *DKK3* knockdown and overexpression treatment group and its control group (5 μmol L^{-1}, Yeasen biotech, China). After the cells were incubated in a 37°C incubator for 30 min, the fresh medium was changed and photographed by laser confocal. The fluorescence intensity in each cell was detected by Zen 2.1 software, and the operation was the same as that of mitochondrial imaging.

Mice intravitreal injections

All mice were housed in an environmentally controlled, pathogen-free barrier facility on a 12-h light-dark cycle, with food and water available. C57BL/6J mice were bred in our laboratory. The mice included an old group (18 months old) and a young group (two months old). According to the weight of the mice, they were anesthetized by intraperitoneal injection of 4% chloral hydrate and treated with tropicamide eye drops. A needle (Dickinson, 30 g×1/2) was used to punch holes in the upper edge of the equatorial part of the mouse eye, and 1 microliter of virus (virus titer: 3×10^{13} vg mL^{-1}) was injected with a micro syringe (syringe, Hamilton No. 7632-01; needle, Hamilton No. 7803-05, including fluorescent indicator), and the needle was taken out after staying in the eye for 10 s. Three months later, the mice were killed by anesthesia for experimental detection.

Retina immunofluorescence

Fixation. The eyeball was fixed in 4% PFA for a short time (about 10 min). Transfer the eyeball to the anatomical microscope, cut a small opening on the cornea with ophthalmic scissors, put it back into the fixing solution, continue to put it on ice for 2 h, and wash it with PBS 3 times.

Dehydration. Place the fixed eyeball in 30% sucrose solution until the eyeball settles to the bottom and dehydration is completed.

Embedding section. Take out the eyeball, cut off the cornea along the equator under the anatomical microscope, carefully clip out the crystal to avoid damaging other parts of the eyeball, and then suck up the liquid. Put it into the embedding box filled with OCT, place it flat at −80°, and freeze it for 30 min. Complete the slicing step on the frozen slicer and select the thickness of 12 μm.

Baking. Select the slice with the ideal slicing effect and bake it at 37°C for 30 min. Take out the film, put it into the immunohistochemical wet box, draw a circle around the tissue block with an oily pen, and wash it with PBS three times for five min each time.

Blocking. Add blocking solution (5% serum, 0.25% TritonX-100+0.06% sodium azide) 50 μL. Incubate for 2 h at room temperature.

Binding of primary antibody. Suck off the blocking solution and add an appropriate proportion of the primary antibody (*DKK3* (protentech, 10365-1-ap, 1:100), rod: rhodopsin (cell signaling technology, #27182, 1:200), cone: arrestin (millipore, ab15282), RGC: Brn3a (Abcam, ab245230, 1:200) , Müller glia Rlbp1 (Abcam, ab243664, 1:200), microglia Iba1 (Proteintech, 10904, 1:2000)). Incubated at 4°C at night, the primary antibody was removed, and PBS was washed three times for five min each time.

Binding of secondary antibodies. Add fluorescent secondary antibodies with an appropriate dilution concentration (1:500), respectively, avoid light, incubate at room temperature for 1 hour, and wash with PBS three times for 5 min each time.

Sealing and observation. Seal the film with a sealing agent containing DAPI and test the results under a laser confocal microscope.

Transmission electron microscopy

Cells were prefixed with a 3% glutaraldehyde, postfixed in 1% osmium tetroxide, dehydrated in series acetone, infiltrated in Epox 812, and embedded. The semi-thin sections were stained with methylene blue, and ultra-thin sections were cut with a diamond knife and stained with uranyl acetate and lead citrate. Sections were examined with a JEM-1400-FLASH Transmission Electron Microscope.

The eyeball was prefixed with a 3% glutaraldehyde, postfixed in 1% osmium tetroxide, dehydrated in series acetone, infilitrated in Epox 812, and embedded. The semithin sections were stained with methylene blue, and ultrathin sections were cut with a diamond knife and stained with uranyl acetate and lead citrate. Sections were examined with a JEM-1400-FLASH Transmission Electron Microscope.

TUNEL staining of eyeball sections

Eyeball slices were fixed with 4% PFA for 10 min at room temperature and moistened with PBS twice. PBS containing 0.3% Triton X-100 was incubated at room temperature for five min. Incubate in 0.3% hydrogen peroxide solution (0.3% H_2O_2 in PBS) was prepared with PBS at room temperature for 20 min, and moistened with PBS three times. According to TDT enzyme 5 μL+Biotin-dUTP 45 μL sample^{-1}, one needs to prepare a biotin labeling solution and incubate at 37°C away from light for 60 min. PBS was moistened once, and 0.2 mL labeled reaction termination solution was added dropwise and incubated at room temperature for 10 min. Streptavidin HRP 1 μL+streptavidin HRP dilution 49 μL sample^{-1} was configured with streptavid in HRP working fluid, incubated in the dark for 30 min at room temperature, and washed with PBS three times. An appropriate amount of DAB chromogenic solution A and DAB chromogenic solution B were mixed in equal volumes, incubated at room temperature for 30 min according to 0.2 mL sample^{-1}, and washed with PBS three times. Hematoxylin dye was dyed at room temperature for 10 min and washed with PBS three times. The staining results were photographed by confocal observation.

Statistics and reproducibility

The data of each experimental group were repeated at least three times. Graphpad Prism 8.0 was used to count the experimental data of each group. The *t*-test and one-way ANOVA provided by the software were used to analyze the differences in the experimental data. *P* values of <0.05 were considered to be significant and indicated by *; *P* values of <0.01 were indicated by ** and *P* values of <0.001 by ***.

Computational methods

Data pre-processing

The Cell Ranger package (v3.1, 10X Genomics) was used to extract unique molecular identifiers, cell barcodes, and genomic reads from the sequencing results of 10X Chromium experiments. Reads were aligned against the annotated human genome (GRCh38), including both protein-coding and non-coding transcripts. Reads with the same cell barcode and unique molecular identifier were collapsed into a unique transcript. The Cell Ranger Package v3.1 algorithm has two key steps. It uses a cutoff based on the total UMI counts of each barcode to identify cells. This step identifies the primary mode of high RNA-content cells. Then, the algorithm uses the RNA profile of each remaining barcode to determine if it is “empty” or a cell-containing partition. This second step captures low RNA content cells whose total UMI counts may be similar to empty GEMs. In the first step, the original Cell Ranger cell calling algorithm is used to identify the primary mode of high RNA content cells,

using a cutoff based on the total UMI count for each barcode. Cell Ranger takes as input the expected number of recovered cells, N (see expect-cells). Let m be the 99th percentile of the top N barcodes by the total UMI counts. All barcodes whose total UMI counts exceed $m/10$ are called cells in the first pass. In the second step, a set of barcodes with low UMI counts that likely represent "empty" GEM partitions is selected. A model of the RNA profile of selected barcodes is created. This model, called the background model, is a multinomial distribution of genes. It uses Simple Good-Turing smoothing to provide a non-zero model estimate for genes that were not observed in the representative empty GEM set. Finally, the RNA profile of each barcode not called a cell in the first step is compared to the background model. Barcodes whose RNA profile strongly disagrees with the background model are added to the set of positive cell calls. This second step identifies cells that are distinguishable from the profile of empty GEMs, even though they may have a much lower RNA content than the largest cells in the experiment. Cells with fewer than 200 or over 10,000 genes detected or a mitochondrial gene ratio and red blood cell marker genes' ratio of greater than 10% were excluded. Doublets were detected using the Scrublet package (version 2.0.2) using the scrub.scrub_doublets () function. The batch effect was corrected with the FindIntegrationAnchors () function of each sample, and then by running the IntegrateData () function.

Cell clustering and sub-clustering

Seurat v3 (Seurat_3.2.0) integration was used for cell clustering. The output of Cell Ranger aggr was loaded into R by using Seurat v3 for a modified integration analysis to remove batch effects and clustering. The Seurat v3 anchoring procedure consists of five broad steps: (1) for each cell, the counts were log normalized (1+counts per 10,000) with the NormalizeData function. Variable genes were selected using the FindVariableGenes function with the default parameters. (2) A shared nearest neighbors graph was constructed based on the Euclidean distance in the low-dimensional subspace spanned by the selected significant principal components. Cells were clustered using the FindClusters function at an appropriate resolution. (3) Cells were visualized using a two-dimensional t-distributed stochastic neighbor embedding (t-SNE) algorithm with the RunTSNE function, and the uniform manifold approximation and projection (UMAP) dimensional reduction algorithm with the RunUMAP function. The TSNE coordinate information of projection_TSNE_SC.csv—or the UMAP coordinate information of projection_UMAP_SC.csv—and the clustering category information of clusters_SC.csv were imported into the Loupe Cell Browser for visualization. (4) Differential expression analysis for each cluster was performed using the Wilcoxon rank-sum test, as implemented in the FindAllMarkers function. We set 0.2–2.0 resolution parameters in the FindAllCluster function. The bimod likelihood ratio statistical test of Seurat V3 was used to screen the specific differential expression genes of different cell groups, which met the requirements of P-value ≤ 0.05 and more than two times the differential expression range to screen the DEGs between the designated and other cell groups. The screening basis of the cell group for specific expression genes is significantly upregulated expression genes belonging to this cell group, not the upregulated expression genes belonging to other cell groups. The thermogram only shows how the top 50 genes rank in terms of the average expression amount of this cell group compared with the different amplitudes of other cell groups. (5) Cell types were assigned to each cluster using the abundance of known marker genes.

The retinal neurons, including horizontals (*ONECUT1*), bipolars (*VSX2*), amacrines (*GAD1* and *GAD2*), and RGCs (*NEFL*, *NEFM*, *RBPMS*, *POU4F1*) have a hierarchical cell type organization, with nested groups of related cells. To identify the cell subtypes of these neurons, we extracted each of these cells and merged all samples for further sub-clustering analysis. The details of the expression of the markers for each cell type across the tissues are listed in Table S1 in Supporting Information.

Cell type annotation

The 10 sets of retina cell markers were rods (*GNAT1*, *NR2E2*, *PDE6G*), cones (*ARR3*, *CNGA3*, *PDE6H*), horizontals (*ONECUT2*), bipolars (*VSX2*, *VSX1*), amacrines (*GAD1*), RGCs (*NEFL*, *NEFM*, *RBPMS*, *POU4F1*), microglia (*AIF1*, *C1QA*, *C1QB*), astrocytes (*GFAP*), Müllers (*RLBP1*), and endothelials (*VWF*, *PECAM1*).

Regional transcriptomic comparative analysis

We performed differential gene expression analysis on each cell type in one region compared to other regions. DEGs in each comparison group of samples (e.g., between the cells from the superior retina and the other five regions) were calculated by FindMarkers(). The average log (fold change) of each DEG (FDR<0.05) was calculated as significant DEGs in that region (regional preferred genes) for pathway enriched analysis using metascape (Zhou et al., 2019) and STRING: functional protein association networks (Szklarczyk et al., 2011).

Transcriptomic comparative analysis across ages

To identify the dynamic changes in gene expression at different stages of development and aging, we used 21, 32, and 44 years as the adult group, and E23rd weeks, P4th days, 7 years, 56 years, 62 years, and 81 years to compare with the adult group, respectively. We performed a DEG analysis on each cell type in the comparing groups. DEGs in each comparison group of samples (e.g., between the cells from

seven years old and the adult group) were calculated with FindMarkers(). The average log (fold change) of each DEG (FDR<0.05) was calculated as significant DEGs in that age (age-preferred genes) for pathway enriched analysis using metascape(Zhou et al., 2019) and STRING: functional protein association networks (Szklarczyk et al., 2011).

Pairwise expression pattern of DEGs across ages

The pairwise distance matrix was calculated using R. This method option calculates all pairwise distances between spatial points (in rows) and presents the distances as a matrix.

Cell-cell communication analysis

The CellChat R package (Jin et al., 2021) was used to infer global communications among retina celltypes, interactions among ligands, receptors, and their cofactors that accurately represent known heteromeric molecular complexes. CellChat classifies signaling pathways and delineates conserved and context-specific pathways across different datasets. Functions of identify OverExpressedGenes(cellchat, thresh. p=0.05), identifyOverExpressedInteractions(cellchat), projectData(cellchat, PPI.human), computeCommunProb(cellchat), computeCommunProbPathway(cellchat), aggregateNet(cellchat), netAnalysis_signalingRole(cellchat, slot.name="netP"), computeNetSimilarity(cellchat, type="functional"), netEmbedding(cellchat, type="functional"), netClustering(cellchat, type="functional"), computeNetSimilarity(cellchat, type="structural"), netEmbedding(cellchat, type="structural") and netClustering(cellchat, type="structural") were used for the retina cell-cell communication analysis of each age.

Regulatory network analysis

SCENIC is a computational method for simultaneous gene regulatory network reconstruction and cell-state identification from single-cell RNA-seq data (Aibar et al., 2017). The SCENIC R package was used to infer gene regulatory networks and cell types from single-cell RNA-seq data of each age and across ages. Briefly, the SCENIC pipeline consists of three steps. First, candidate regulatory modules are inferred from the co-expression patterns between genes. Next, co-expression modules are refined by eliminating indirect targets using TF motif information. Finally, the activity of these discovered regulons is measured in each cell and used for clustering. We then clustered cells using the SCENIC output file "3.7_binaryRegulonActivity_noDupl.RData" with the modified "clustering-and-classification" algorithm (Lake et al., 2016). The algorithm was slightly modified, i.e., overdispersed genes were not chosen, and all regulons were used to perform unsupervised clustering. We used a standard area under the curve (AUC) classifier to identify cell type-specific markers (DEGs among different cell types). The function FindAllMarkers in the R package Seurat 3.0. Markers was selected only if the average difference of the log2-transformed with FDR<0.05.

Compliance and ethics *The author(s) declare that they have no conflict of interest.*

Acknowledgements *This work was supported by the National Natural Science Foundation of China (81790643, 81970839, 82271105, 82121003), the Sichuan Science and Technology Program (2021YFS0033, 2021YFS0369, 2021YFS0404, 2021JDGD0036) and the Chinese Academy of Medical Sciences (CAMS) Innovation Fund for Medical Sciences (2019-I2M-5-032).*

References

Aibar, S., González-Blas, C.B., Moerman, T., Huynh-Thu, V.A., Imrichova, H., Hulselmans, G., Rambow, F., Marine, J.C., Geurts, P., Aerts, J., et al. (2017). SCENIC: single-cell regulatory network inference and clustering. Nat Methods 14, 1083–1086.

Baffet, A.D., Hu, D.J., and Vallee, R.B. (2015). Cdk1 activates pre-mitotic nuclear envelope dynein recruitment and apical nuclear migration in neural stem cells. Dev Cell 33, 703–716.

Bonnel, S., Mohand-Said, S., and Sahel, J.A. (2003). The aging of the retina. Exp Gerontol 38, 825–831.

Boycott, B.B., and Wässle, H. (1991). Morphological classification of bipolar cells of the primate retina. Eur J Neurosci 3, 1069–1088.

Clark, B.S., Stein-O'Brien, G.L., Shiau, F., Cannon, G.H., Davis-Marcisak, E., Sherman, T., Santiago, C.P., Hoang, T.V., Rajaii, F., James-Esposito, R.E., et al. (2019). Single-cell RNA-Seq analysis of retinal development identifies NFI factors as regulating mitotic exit and late-born cell specification. Neuron 102, 1111–1126.e5.

Correia-Melo, C., Marques, F.D.M., Anderson, R., Hewitt, G., Hewitt, R., Cole, J., Carroll, B.M., Miwa, S., Birch, J., Merz, A., et al. (2016). Mitochondria are required for pro-ageing features of the senescent phenotype. EMBO J 35, 724–742.

Cowan, C.S., Renner, M., De Gennaro, M., Gross-Scherf, B., Goldblum, D., Hou, Y., Munz, M., Rodrigues, T.M., Krol, J., Szikra, T., et al. (2020). Cell types of the human retina and its organoids at single-cell resolution. Cell 182, 1623–1640.e34.

Deng, Y., Qiao, L., Du, M., Qu, C., Wan, L., Li, J., and Huang, L. (2022). Age-related macular degeneration: epidemiology, genetics, pathophysiology, diagnosis, and targeted therapy. Genes Dis 9, 62–79.

Fan, Z., Beresford, P.J., Zhang, D., and Lieberman, J. (2002). HMG2 interacts with the nucleosome assembly protein SET and is a target of the cytotoxic T-lymphocyte protease granzyme A. Mol Cell Biol 22, 2810–2820.

Fletcher, A.E. (2010). Free radicals, antioxidants and eye diseases: evidence from epidemiological studies on cataract and age-related macular degeneration. Ophthal Res 44, 191–198.

Harman, A., Abrahams, B., Moore, S., and Hoskins, R. (2000). Neuronal density in the human retinal ganglion cell layer from 16-77 years. Anat Rec 260, 124–131.

Harman, D. (1981). The aging process. Proc Natl Acad Sci USA 78, 7124–7128.

Hoshino, A., Ratnapriya, R., Brooks, M.J., Chaitankar, V., Wilken, M.S., Zhang, C., Starostik, M.R., Gieser, L., La Torre, A., Nishio, M., et al. (2017). Molecular anatomy of the developing human retina. Dev Cell 43, 763–779.e4.

Hu, Y., Wang, X., Hu, B., Mao, Y., Chen, Y., Yan, L., Yong, J., Dong, J., Wei, Y., Wang, W., et al. (2019). Dissecting the transcriptome landscape of the human fetal neural retina and retinal pigment epithelium by single-cell RNA-seq analysis. PLoS Biol 17, e3000365.

Huang, L., Chen, Y., Lin, Y., Tam, P.O.S., Cheng, Y., Shi, Y., Gong, B., Lu, F., Yang, J., Wang, H., et al. (2019). Genome-wide analysis identified

17 new loci influencing intraocular pressure in Chinese population. Sci China Life Sci 62, 153–164.
Huang, L., Fang, L., Liu, Q., Torshizi, A.D., and Wang, K. (2022). Integrated analysis on transcriptome and behaviors defines HTT repeat-dependent network modules in Huntington's disease. Genes Dis 9, 479–493.
Huang, L., Zhang, H., Cheng, C.Y., Wen, F., Tam, P.O.S., Zhao, P., Chen, H., Li, Z., Chen, L., Tai, Z., et al. (2016). A missense variant in FGD6 confers increased risk of polypoidal choroidal vasculopathy. Nat Genet 48, 640–647.
Isik, S., Zaim, M., Yildiz, M.T., Negis, Y., Kunduraci, T., Karakas, N., Arikan, G., and Cetin, G. (2015). DNA topoisomerase IIβ as a molecular switch in neural differentiation of mesenchymal stem cells. Ann Hematol 94, 307–318.
Jin, S., Guerrero-Juarez, C.F., Zhang, L., Chang, I., Ramos, R., Kuan, C.H., Myung, P., Plikus, M.V., and Nie, Q. (2021). Inference and analysis of cell-cell communication using CellChat. Nat Commun 12, 1088.
Kaneko, A. (1970). Physiological and morphological identification of horizontal, bipolar and amacrine cells in goldfish retina. J Physiol 207, 623–633.
Kolb, H., Fernandez, E., and Nelson, R. (2020). Webvision: The Organization of the Retina and Visual System. 1–1839.
Kolb, H., Linberg, K.A., and Fisher, S.K. (1992). Neurons of the human retina: a Golgi study. J Comp Neurol 318, 147–187.
Kummer, E., and Ban, N. (2021). Mechanisms and regulation of protein synthesis in mitochondria. Nat Rev Mol Cell Biol 22, 307–325.
Lake, B.B., Ai, R., Kaeser, G.E., Salathia, N.S., Yung, Y.C., Liu, R., Wildberg, A., Gao, D., Fung, H.L., Chen, S., et al. (2016). Neuronal subtypes and diversity revealed by single-nucleus RNA sequencing of the human brain. Science 352, 1586–1590.
Li, W., Cheng, H., Li, G., and Zhang, L. (2020). Mitochondrial damage and the road to exhaustion. Cell Metab 32, 905–907.
Lian, G., Wong, T., Lu, J., Hu, J., Zhang, J., and Sheen, V. (2019). Cytoskeletal associated filamin A and RhoA affect neural progenitor specification during mitosis. Cerebral Cortex 29, 1280–1290.
Liao, N., Li, C., Jiang, H., Fang, A., Zhou, S., and Wang, Q. (2016). Neovascular glaucoma: a retrospective review from a tertiary center in China. BMC Ophthalmol 16, 14.
Lin, M.T., and Beal, M.F. (2006). Mitochondrial dysfunction and oxidative stress in neurodegenerative diseases. Nature 443, 787–795.
Lu, Y., Shiau, F., Yi, W., Lu, S., Wu, Q., Pearson, J.D., Kallman, A., Zhong, S., Hoang, T., Zuo, Z., et al. (2020). Single-cell analysis of human retina identifies evolutionarily conserved and species-specific mechanisms controlling development. Dev Cell 53, 473–491.e9.
Lukowski, S.W., Lo, C.Y., Sharov, A.A., Nguyen, Q., Fang, L., Hung, S.S., Zhu, L., Zhang, T., Grünert, U., Nguyen, T., et al. (2019). A single-cell transcriptome atlas of the adult human retina. EMBO J 38, e100811.
Macneil, M.A., Heussy, J.K., Dacheux, R.F., Raviola, E., and Masland, R. H. (1999). The shapes and numbers of amacrine cells: matching of photofilled with Golgi-stained cells in the rabbit retina and comparison with other mammalian species. J Comp Neurol 413, 305–326.
MacNeil, M.A., and Masland, R.H. (1998). Extreme diversity among amacrine cells: implications for function. Neuron 20, 971–982.
Macosko, E.Z., Basu, A., Satija, R., Nemesh, J., Shekhar, K., Goldman, M., Tirosh, I., Bialas, A.R., Kamitaki, N., Martersteck, E.M., et al. (2015). Highly parallel genome-wide expression profiling of individual cells using nanoliter droplets. Cell 161, 1202–1214.
Masland, R. (2001). Neuronal diversity in the retina. Curr Opin Neurobiol 11, 431–436.
Masland, R.H. (2012). The neuronal organization of the retina. Neuron 76, 266–280.
Mellough, C.B., Bauer, R., Collin, J., Dorgau, B., Zerti, D., Dolan, D.W.P., Jones, C.M., Izuogu, O.G., Yu, M., Hallam, D., et al. (2019). An integrated transcriptional analysis of the developing human retina. Development 146.
Nomura, Y., Mulavara, A.P., Richards, J.T., Brady, R., and Bloomberg, J.J. (2005). Optic flow dominates visual scene polarity in causing adaptive modification of locomotor trajectory. Cogn Brain Res 25, 624–631.
Novichkov, P.S., Rodionov, D.A., Stavrovskaya, E.D., Novichkova, E.S., Kazakov, A.E., Gelfand, M.S., Arkin, A.P., Mironov, A.A., and Dubchak, I. (2010). RegPredict: an integrated system for regulon inference in prokaryotes by comparative genomics approach. Nucl Acids Res 38, W299–W307.
Peng, Y.R., Shekhar, K., Yan, W., Herrmann, D., Sappington, A., Bryman, G.S., van Zyl, T., Do, M.T.H., Regev, A., and Sanes, J.R. (2019). Molecular classification and comparative taxonomics of foveal and peripheral cells in primate retina. Cell 176, 1222–1237.e22.
Reichenbach, A., and Bringmann, A. (2020). Glia of the human retina. Glia 68, 768–796.
Shen, Y., Shen, H., Guo, D., Sun, X., Sun, Y., Hong, N., Wang, X., Xie, C., Zhao, Y., He, Q., et al. (2020). Recent developments in regenerative ophthalmology. Sci China Life Sci 63, 1450–1490.
Stephenson, J., Nutma, E., van der Valk, P., and Amor, S. (2018). Inflammation in CNS neurodegenerative diseases. Immunology 154, 204–219.
Szél, A., Lukáts, A., Fekete, T., Szepessy, Z., and Röhlich, P. (2000). Photoreceptor distribution in the retinas of subprimate mammals. J Opt Soc Am A 17, 568–579.
Szklarczyk, D., Franceschini, A., Kuhn, M., Simonovic, M., Roth, A., Minguez, P., Doerks, T., Stark, M., Muller, J., Bork, P., et al. (2011). The STRING database in 2011: functional interaction networks of proteins, globally integrated and scored. Nucl Acids Res 39, D561–D568.
Takahashi, K., and Yamanaka, S. (2006). Induction of pluripotent stem cells from mouse embryonic and adult fibroblast cultures by defined factors. Cell 126, 663–676.
Ugrinova, I., Pashev, I.G., and Pasheva, E.A. (2009). Nucleosome binding properties and Co-remodeling activities of native and *in vivo* acetylated HMGB-1 and HMGB-2 proteins. Biochemistry 48, 6502–6507.
Ungvari, Z., Tarantini, S., Kiss, T., Wren, J.D., Giles, C.B., Griffin, C.T., Murfee, W.L., Pacher, P., and Csiszar, A. (2018). Endothelial dysfunction and angiogenesis impairment in the ageing vasculature. Nat Rev Cardiol 15, 555–565.
Vasiljevic, A., Champier, J., Figarella-Branger, D., Wierinckx, A., Jouvet, A., and Fèvre-Montange, M. (2013). Molecular characterization of central neurocytomas: potential markers for tumor typing and progression. Neuropathology 33, 149–161.
Wang, S., Poli, S., Liang, X., and Peng, G.H. (2021a). Longitudinal single-cell RNA-seq of hESCs-derived retinal organoids. Sci China Life Sci 64, 1661–1676.
Wang, S., Zheng, Y., Li, Q., He, X., Ren, R., Zhang, W., Song, M., Hu, H., Liu, F., Sun, G., et al. (2021b). Deciphering primate retinal aging at single-cell resolution. Protein Cell 12, 889–898.
Wei, Y.H., Ma, Y.S., Lee, H.C., Lee, C.F., and Lu, C.Y. (2001). Mitochondrial theory of aging matures-roles of mtDNA mutation and oxidative stress in human aging. Chin Med J 64, 259–270.
Whitmore, S.S., Wagner, A.H., DeLuca, A.P., Drack, A.V., Stone, E.M., Tucker, B.A., Zeng, S., Braun, T.A., Mullins, R.F., and Scheetz, T.E. (2014). Transcriptomic analysis across nasal, temporal, and macular regions of human neural retina and RPE/choroid by RNA-Seq. Exp Eye Res 129, 93–106.
Yang, Z.R., Dong, W.G., Lei, X.F., Liu, M., and Liu, Q.S. (2012). Overexpression of Dickkopf-3 induces apoptosis through mitochondrial pathway in human colon cancer. World J Gastroenterol 18, 1590–1601.
Yaqoob, P. (2017). Ageing alters the impact of nutrition on immune function. Proc Nutr Soc 76, 347–351.
Zepeda-Romero, L.C., Vazquez-Membrillo, M., Adan-Castro, E., Gomez-Aguayo, F., Gutierrez-Padilla, J.A., Angulo-Castellanos, E., Barrera de Leon, J.C., Gonzalez-Bernal, C., Quezada-Chalita, M.A., Meza-Anguiano, A., et al. (2017). Higher prolactin and vasoinhibin serum levels associated with incidence and progression of retinopathy of prematurity. Pediatr Res 81, 473–479.
Zhang, F., Kurokawa, K., Lassoued, A., Crowell, J.A., and Miller, D.T. (2019). Cone photoreceptor classification in the living human eye from

photostimulation-induced phase dynamics. Proc Natl Acad Sci USA 116, 7951–7956.
Zhao, B., Liu, P., Fukumoto, T., Nacarelli, T., Fatkhutdinov, N., Wu, S., Lin, J., Aird, K.M., Tang, H.Y., Liu, Q., et al. (2020). Topoisomerase 1 cleavage complex enables pattern recognition and inflammation during senescence. Nat Commun 11, 908.
Zhou, S., Zhu, Y., Mashrah, M., Zhang, X., He, Z., Yao, Z., Zhang, C., Guo, F., Hu, Y., and Zhang, C. (2017). Expression pattern of DKK3, dickkopf WNT signaling pathway inhibitor 3, in the malignant progression of oral submucous fibrosis. Oncol Rep 37, 979–985.
Zhou, Y., Zhou, B., Pache, L., Chang, M., Khodabakhshi, A.H., Tanaseichuk, O., Benner, C., and Chanda, S.K. (2019). Metascape provides a biologist-oriented resource for the analysis of systems-level datasets. Nat Commun 10, 1523.

SUPPORTING INFORMATION

The supporting information is available online at http://doi.org/10.1007/s11427-021-2163-1. The supporting materials are published as submitted, without typesetting or editing. The responsibility for scientific accuracy and content remains entirely with the authors.